Association between power law coefficients of the anatomical noise power spectrum and lesion detectability in breast imaging modalities

Lin Chen[1], **Craig K. Abbey**[2], and **John M. Boone**[1,3]
[1]Department of Biomedical Engineering, University of California Davis

[2]Department of Psychology, University of California Santa Barbara

[3]Department of Radiology, University of California Davis

Abstract

Purpose—Previous research has demonstrated that a parameter extracted from a power function fit to the anatomical noise power spectrum, β, may be predictive of breast mass lesion detectability in x-ray based medical images of the breast. In this investigation, the value of β was compared with a number of other more widely used parameters, in order to determine the relationship between β and these other parameters.

Methods—This study made use of breast CT data sets, acquired on two breast CT systems developed in our laboratory. A total of 185 breast data sets in 183 women were used, and only the unaffected breast was used (where no lesion was suspected). The anatomical noise power spectrum was computed from two-dimensional regions of interest (ROI), was fit to a power function (NPS(f) = $\alpha f^{-\beta}$), and the exponent parameter (β) was determined using log/log linear regression. Breast density for each of the volume data sets was characterized in previous work. The breast CT data sets analyzed in this study were part of a previous study which evaluated the receiver operating characteristic (ROC) curve performance using simulated spherical lesions and a pre-whitened matched filter computer observer. This ROC information was used to compute the detectability index as well as the sensitivity at 95% specificity. The fractal dimension was computed from the same ROI's which were used for the assessment of β. The value of β was compared to breast density, detectability index, sensitivity, and fractal dimension, and the slope of these relationships was investigated to assess statistical significance from zero slope. A statistically significant non-zero slope was considered to be a positive association in this investigation.

Results—All comparisons between β and breast density, detectability index, sensitivity at 95% specificity, and fractal dimension demonstrated statistically significant association with $p < 0.001$ in all cases. The value of β was also found to be associated with patient age and breast diameter, parameters both related to breast density. In all associations between other parameters, lower values of β were associated with increased breast cancer detection performance. Specifically, lower values of β were associated with lower breast density, higher detectability index, higher sensitivity, and lower fractal dimension values.

Conclusions—While causality was not and probably cannot be demonstrated, the strong, statistically significant association between the β metric and the other more widely used

Corresponding Author: John M. Boone, Ph.D., FAAPM, FSBI, FACR, Professor of Radiology, UC Davis Medical Center, Ellison Ambulatory Care Center, 4860 Y Street, Sacramento, CA 95817, john.boone@ucdmc.ucdavis.edu.

parameters suggest that β may be considered as a surrogate measure for breast cancer detection performance. These findings are specific to breast parenchymal patterns and mass lesions only.

Introduction

The detection of breast cancer using medical imaging technology is the primary screening approach for breast cancer in most developed countries. While mammography has been the primary screening tool for a number of decades, other modalities such as breast tomosynthesis, breast ultrasound, and breast MRI are also used clinically in various settings for breast cancer screening. Breast CT (bCT) is also being evaluated at a number of institutions around the world for its potential role in breast cancer screening (Mettivier et al., 2011, Weigel et al., 2011). As with all medical imaging procedures, the probability of detecting breast lesions in medical images is related to the signal to noise ratio of the lesion. Sources of noise for x-ray based modalities include x-ray quantum noise, but in the last decade it has become increasingly evident that the anatomical noise of the normal breast parenchyma plays an important role in potentially obscuring the visibility of a breast lesion. While overall noise amplitude is important, the spectral frequency of the noise as characterized by the noise power spectrum also plays an important role in the detectability of a lesion.

Burgess (Burgess et al., 2001a), Bochud (Bochud et al., 1999), and others (Heine et al., 1999) have defined the total noise power spectrum, $NPS_t(f)$, as the sum of the anatomical noise power spectrum, $NPS_a(f)$, and the quantum noise power spectrum, $NPS_q(f)$,:

$$NPS_t(f) = NPS_q(f) + NPS_a(f) \quad \text{Equation 1}$$

The quantum noise power spectrum is a fundamental analytical tool in detector design, development, and assessment, and has been used extensively in the evaluation of x-ray based medical imaging systems (Yang et al., 2008, Miéville et al.). The anatomical noise power spectrum has been discussed in a more limited manner (Bochud et al., 1999, Burgess, 1999, Metheany et al., 2008). It has been observed by Burgess (Burgess, 1999, Burgess et al., 2001b) and others (Bochud et al., 1999, Metheany et al., 2008) that the anatomical noise power spectrum has a reasonable adherence to a power law, for example:

$$NPS_a(f) = \alpha f^{-\beta} \quad \text{Equation 2}$$

This observation is consistent with the broader literature in vision science, where the noise power spectrum of many natural scenes also obeys a power-law relationship (Field, 1987, Burton and Moorhead, 1987, Tolhurst et al., 1992, Ruderman, 1994, van der Schaaf and van Hateren, 1996).

The primary objectives of this study were to evaluate the parameter β in Equation 2, in terms of how it relate to other breast cancer detection performance metrics. In a previous investigation, we demonstrated that the value of β differed between breast imaging modalities including digital mammography, breast tomosynthesis, and breast CT (Chen et al., 2012). Burgess et al (Burgess et al., 2001b, Burgess and Judy, 2007) suggested that the value of β was a measure of breast cancer detection performance, and they predicted that smaller values of β would result in better screening performance. In Metheany *et al.* (Metheany et al., 2008), an analytical derivation demonstrated that the value of β for tomographic imaging, β_{CT}, was related to that of two-dimensional mammography, β_{mammo}, by the relationship:

$$\beta_{\text{CT}} = \beta_{\text{mammo}} - 1 \quad \text{Equation 3}$$

The validity of the relationship given in Equation 3 was recently demonstrated experimentally (Heine and Velthuizen, 2002, Chen et al., 2012).

There are two important classes of lesions that can lead to the identification of breast cancer, soft tissue or *mass* lesions, and microcalcifications. While microcalcification detection is a key element in any breast cancer screening environment, the current investigation is mainly focused on the detectability of mass lesions.

Methods

Patient Selection

In addition to initial volunteers, patients with positive mammographic findings (BIRADS 4 or 5) were recruited for imaging with breast CT, and informed consent was obtained under several IRB approved protocols at our institution. A total of 216 participants, 214 patients and 2 volunteers, who ranged in age from 35 to 80 (mean 54 years, $\sigma = 9.5$ years), were enrolled and included in this analysis. Breast CT images were acquired immediately prior to scheduled breast biopsy (except for the two volunteers, who did not have biopsies). The vast majority of patients had both breasts imaged – the breast which contained the suspicious region (the *affected* breast), as well as the unaffected breast. Because this study focuses on the anatomical noise in the background and not signal characteristics, only images of the unaffected breast were included to avoid any bias due to the influence of lesions. Overall, a total of 185 single breast data sets were used in this analysis. Excluding the 4 breast data sets from the two volunteers, the BIRADS breast densities of the remaining 181 women were fatty (10.8% [20]), 25.4% (47) were scattered, 40.0% (74) were heterogeneous, and 21.6% (40) were extremely dense.

Imaging Systems

Two dedicated breast CT scanners, were developed at our institution for the purpose of studying the potential of breast CT for cancer detection. The technical details of these scanners have been described previously (Lindfors et al., 2008). Briefly, both scanners were designed to image the breast with the patient prone on the table top, with the breast to be imaged hanging through a hole in the table. Under the table, a CT gantry is rotated using a combined servomotor, bearing, and angle encoder system (Kollmorgen, Radford, VA). An x-ray tube (Comet AG, Flamatt, Switzerland) and indirect detection CsI-based flat panel detector (PaxScan 4030CB, Varian Medical Systems, Palo Alto, CA) were rotated >360 degrees around the pendant breast, acquiring > 500 projection images. Most CT systems use a full 360° rotation around the object being scanned when that is possible; cardiac and other rapid scanning applications are an exception to this. Full 360° rotation is important in cone beam scanners including the breast CT system. Patients were imaged using 80 kV, with the x-ray tube current (mA) selected based on the breast cup size such that the mean glandular dose of the bCT scans was approximately equal to that of two-view mammography for each woman. The procedure was performed during breath hold, and required approximately 17 seconds. A cone-beam filtered backprojection CT reconstruction algorithm (Feldkamp et al., 1984, Kak and Slaney, 1988) generated 512×512 bCT images using a Shepp–Logan filter. Each reconstructed image was calibrated to Hounsfield units. The average slice thickness in the natively reconstructed coronal images was 0.23 mm ($\sigma = 0.041$ mm), and ranged from 0.18 to 0.41 mm per slice. Pixel dimensions of the coronal images ranged from 0.20 to 0.44 mm, depending on breast size, with an average pixel dimension of 0.35 mm ($\sigma = 0.035$ mm) in coronal images.

Breast CT Segmentation

An automatic method for image segmentation was developed for the bCT images (Packard and Boone, 2007, Nelson et al., 2008, Packard et al., 2012). For each bCT volume data set, the first and last acceptable coronal bCT images were manually identified and tallied as part of the segmentation process. This manual step avoided artifactual images in the posterior breast (including the elimination of implants from the considered field of view), and avoided the nipple anteriorly. The voxels corresponding to air were identified by simple thresholding. A 2-means clustering algorithm was used to segment glandular and adipose tissues based on the image histogram. The estimation process was performed iteratively in conjunction with a seven-point 3D median filter applied to the breast volume. Iteration completed when the glandular fraction estimate converged. The adipose tissue in each slice was flattened by a 2D parabolic correction and smoothed by an adaptive smoothing algorithm. Skin was segmented using the high signal to noise ratio (SNR) air/tissue interface. For each breast CT data set, the voxels were segmented into five categories: air, adipose tissue, glandular tissue, chest-wall and skin. The volume glandular fraction of the breast was computed using (Yaffe et al., 2009, Huang et al., 2011):

$$VGF = \frac{V_{glandular}}{V_{glandular} + V_{adipose}} \times 100\% \quad \text{Equation 4}$$

$V_{glandular}$ and $V_{adipose}$ correspond to the total volume of voxels marked through the segmentation process as glandular and adipose voxels, respectively.

The segmented breast images were also useful in estimating the breast effective diameter (Huang et al., 2011). The breast effective diameter was computed as $D_{eff} = 2\sqrt{A/\pi}$ for each CT image, where $A = N \Delta^2_{pix}$, and where the number of pixels in each image in which there was either adipose or glandular tissue was N, and Δ_{pix} was the pixel dimension. The effective breast diameter at the chest-wall, $D_{chest-wall}$, was determined by averaging the diameters of the first five posterior coronal images adjacent to the manually segmented posterior border.

Assessment of Parameter β

The $NPS_a(f)$ of each breast data set was evaluated using 1000 region of interests (ROIs) in the coronal view, at randomly selected (x, y) locations and at randomly selected slice (z) locations. A rejection method was used to insure that all ROIs were located within the breast anatomy on the image. The ROI was placed on the image based on random-number generated position values, and all pixels in the ROIs were evaluated to assure that none were positioned outside the breast, based upon the segmented images. Once a ROI was determined to be within the breast parenchyma, it was marked graphically on the breast image. Human visional assessment for the ROIs was used to further assure that proper ROI positioning was achieved. For each 64 × 64 pixel ROI, the mean Hounsfield unit was subtracted to obtain zero-mean ROIs of anatomical noise. A 2D Hanning window function [H(r) = 0; r > ½ s , H(r) = ½ + ½ cos(2πr/s), elsewhere] was applied to suppress spectral leakage. $NPS_a(f)$ were estimated by averaging the magnitude squared of the 2D Fast Fourier transform (FFT) from the ROIs. ROIs were selected as a 64 ×64 pixel matrix, with corresponding dimensions on the breast CT images ranging from 13.0 mm to 28.1 mm in side length for the coronal view. The 2D NPS, denoted as $NPS(f_x, f_y)$ was computed by 2D Fourier Transform for each ROI, and the mean noise power spectrum, $\overline{NPS}(f_x, f_y)$, was determined by averaging the NPS from the 1000 ROIs in each volume data set. The one dimensional anatomical noise power spectrum, $NPS_a(f)$, was computed by radially averaging

the 2D $\overline{NPS}(f_x, f_y)$ by using $f_r = \sqrt{f_x^2 + f_y^2}$, with frequency bins of 1/50th f the Nyquist frequency.

In order to compute α and β in Equation 2, the natural logarithm of both NPS_a and f_r was computed, and linear regression was performed on the log/log data to obtain α and β. To avoid NPS anomalies at low frequencies and to avoid the influence of quantum noise at high frequencies (Metheany et al., 2008, Burgess et al., 2001b), the linear regression procedure was performed iteratively, iterating over a range of low frequency endpoints f_1 and over a high frequency range of endpoints f_2. The optimal frequency window (from f_1 to f_2) was selected for each $NPS_a(f)$ as that which maximized R^2, and the values of α and β were then recorded for each breast data set. Other studies (not reported) have demonstrated that the effects of quantum noise, including the influence of the reconstruction kernel, are found above the high-frequency threshold f_2, with negligible influence on the value of β.

The impact of slice thickness was assessed in this investigation. In addition to assessing the noise power for thin section breast CT images (0.23 mm average thickness), the breast CT data sets were averaged to produce thick section (44.3 mm average thickness) "projection" images. Previous studies (Chen et al., 2012) showed that integrating the inherently thin breast CT images produced anatomical noise metrics (β) similar to projection mammograms and tomosynthesis images.

Association between β and age or breast diameter

Age (in years) was recorded for all patients. The relationship between β and age was assessed across a number of age categories: age (patient percentile) <=40 (6.5%), 41–43 (5.9%), 44–46 (9.7%), 47–49 (13.5%), 50–52 (7.6%), 53–55 (13.5%), 56–58 (12.4%), 59–61 (9.2%), 62–64 (7.0%), 65–67 (5.4%), 68–70 (2.7%), and >=71 (6.5%). The age and β in each category were independently averaged. In addition, 158 breast datasets had both breast diameter (at the chest-wall) and β calculated. Data were binned as breast diameter (patient percentile): <10 cm (7.0%), 10–11 cm (9.5%), 11–11.5 cm (8.2%), 11.5–12 cm (8.2%), 12–12.5 cm (10.8%), 12.5–13 cm (8.2%), 13–13.5 cm (10.1%), 13.5–14 cm (11.4%), 14–14.5 cm (5.7%), 14.5–15 cm (7.6%), 15–15.5 cm (8.9%), >15.5 cm (4.4%). Similarly, both breast diameters and β were independently averaged in each category for comparison.

Breast CT Detectability Simulation

An observer performance model was developed previously (Packard et al., 2012) to simulate the computer observer detection performance in breast CT images. For each bCT volume (512 × 512 × N voxels, N ranged from ~200 to 512 depending on breast size), simulated spherical mass lesions of diameter 1, 2, 3 and 5 mm were generated and randomly inserted within the breast parenchyma. Projections of the breast CT data containing the lesion were generated from the reconstructed bCT data sets, in the coronal, sagittal and axial planes. Using signal-known-exactly (SKE) model observer methodology, the receiver operating characteristic (ROC) curve was determined on the projected images of various thicknesses, using a pre-whitened matched filter (PWMF) based model observer. The details of this study were reported previously (Packard and Boone, 2007, Packard et al., 2012). Briefly, for the given projection thickness, viewing plane, and breast volume, 500 ROIs of 64 × 64 pixels with simulated lesions and 500 ROIs "non-lesions" were sampled with the PWMF to produce a set of 1000 responses, from which the ROC curve was generated. The area under the ROC curve (AUC) and the sensitivity at a specificity of 95% were evaluated from the computed ROC curves (Packard et al., 2012, Lindfors et al., 2008).

Under the general assumption of a two-alternative forced-choice study (2AFC), the proportion of correct responses, Pc, is equivalent to AUC. This is monotonically related to the detectability index (Barrett and Myers, 2004)

$$d_A = \sqrt{2}\Phi^{-1}(P_c) = 2\mathrm{ERF}^{-1}(2AUC - 1) \quad \text{Equation 5}$$

where Φ^{-1} is the inverse cumulative normal function and ERF^{-1} is the inverse error function. In this study, the dependence of β is presented in terms of the detectability index d_A, understanding that this is a surrogate measure of observer performance.

Fractal Dimension

To calculate the fractal dimension, the conventional box-counting technique (Boone et al., 1998, Cargill et al., 1991) was adopted. The fractal dimension D was calculated from the slope of log/log $A(\varepsilon)$ versus ε as:

$$D = 2 - \frac{\Delta\log[A(\varepsilon)]}{\Delta\log(\varepsilon)} \quad \text{Equation 6}$$

where $A(\varepsilon)$ is the surface area of ROI at an effective pixel size ε. For a given ROI, the surface area $A(\varepsilon)$ was calculated as:

$$A(\varepsilon) = \sum_{x,y}\varepsilon^2 + \sum \varepsilon(|i_\varepsilon(x,y) - i_\varepsilon(x,y+1)| + |i_\varepsilon(x,y) - i_\varepsilon(x+1,y)|) \quad \text{Equation 7}$$

where $i_\varepsilon(x,y)$ corresponds to the Hounsfield unit at pixel (x,y). In this study, the same ROIs were used for the α and β calculations. For each 64×64 pixel ROIs different effective pixel sizes were synthesized by averaging adjacent pixels. Accordingly, five pairs of A(ε)/ε values were obtained from binning 1×1, 2×2, 4×4, 8×8, and 16×16 pixels for each ROI, and then linear regression was used to determine the slope of log (A(ε)) versus log(ε), in order to calculate the fractal dimension D. Each calculation iterated over the 1000 ROIs for each breast (as previously described), and the fractal dimension was determined by averaging the fractal dimension over all ROIs for each bCT data set.

Results

Figure 1 illustrates an example of determining the value of β from breast anatomy, for thin slice images. Figure 1(b) shows the averaged two dimensional NPS. Radial averaging extracted the 1D *NPS*, which was plotted on a log-log axis as a function of radial spatial frequency f_r, as shown in Figure 1(c). The 1D NPS curve was generated by averaging the frequency points in the 2D NPS (Figure 1b) into 50 different bins, from f=0 to the Nyquist frequency. Previous research has shown that the NPS_a dominates in the low frequency region of the NPS, while quantum noise dominates at the highest frequencies. The dots (◆) in Figure 1(c) represent the $NPS_a(f_r)$ data, and the power-law relationship was computed over a defined frequency range. For the images illustrated in Figure 1, the maximum R^2 was obtained at a frequency range from 0.08 mm^{-1} to 0.45 mm^{-1}, and the corresponding β was computed as 1.86 for this illustrative data set. For all 185 breast image datasets included in this investigation, the frequency bounds for each breast were varied slightly, all spanning the frequency range from 0.04 to 0.61 mm^{-1}. The R^2 measured across all the breasts averaged to > 0.990 in all cases. The average value of β for all the 185 breast image sets was 1.96 on bCT coronal plane, with a standard deviation of 0.46.

The value of β was assessed for the thick, projection views in a similar manner. Due to limitations in identifying the thicker projection data, 105 data sets were used for the

projection image cases in the axial view, which corresponds roughly to the cranial caudal (CC) mammographic projection. The average value of β corresponding to thick projections was 3.15, with a standard deviation of 0.50.

The values of β, computed from the thin section coronal breast CT data sets, were characterized statistically in terms of their association with volume glandular fraction (VGF), patient age, and diameter of breast. There were 159 breast image datasets having both VGF and β calculated in common (Figure 2), and β is observed to increase as a function of $\log_e$(VGF), with an R^2 of 0.35. To determine if there was a statistically significant relationship between β and $\log_e$(VGF), regression analysis was performed testing the null hypothesis that the overall slope is zero. The *p*-value was computed (*p*<0.0001) under T-test, which suggests that the slope of the linear regression line (β versus $\log_e$(VGF)), differs significantly from 0. Therefore, there is a strong statistical association between these two parameters.

Similar analyses were performed between age and β, and between breast diameter (measured at the chest-wall) and β. Figure 3(a) illustrates the age-dependent trend of β, and Figure 3(b) illustrates the relationship between breast diameter and β. Error bars in each plot correspond to one standard deviation. Linear regression results are shown on each figure, with R^2 reported as 0.41 across age and β (Figure 3a), and 0.75 across breast diameter and β (Figure 3b). Statistical evaluation of the slope of these two regression lines showed high statistical association between age and β (N = 185 breasts, *p* = 0.0027), and also between breast diameter and β (N = 158 breasts, *p* = 0.00011). These *p*-values also suggested that a linear relationship between the parameters is plausible.

Detectability Index values were generated from computer observer experiments which placed simulated spherical tumors of different sizes as 1 mm, 2 mm, 3 mm and 5 mm into real breast backgrounds measured using breast CT. The relationship between β and the detectability index were estimated using both thin section images and thick projection images. Figures 4 through 7 illustrate the relationship between β and detectability index with tumor diameters of 1, 2, 3, and 5 mm, respectively. The (a) component of Figures 4 – 7 correspond to thin section (breast CT) coronal images, and the (b) component of these figures demonstrate the relationships for thick projection images (mammogram-like) for the axial projection. Cases with AUC=1 and a corresponding detectability index of ∞ were excluded. Table 1 shows the number of data sets used, the R^2 value, and the *p*-value generated for each lesion diameter (1 mm, 2 mm, 3 mm, and 5 mm) and for the thin and thick section images. Figures 4, 5, 6, and 7 along with Table 1 demonstrate that there is a strong statistical relationship between the detectability index (defined in Equation 5) and β. In all comparisons, *p* < 0.0001.

The area under the ROC curve (AUC) is a traditional measure of detection performance in imaging science, however in clinical breast imaging radiologists tend to limit their operating points to a specific region on the ROC curve corresponding to a compromise between sensitivity and call-back rate (which is strongly related to specificity given the low disease prevalence). This operating point is approximately near the 95% specificity point, corresponding to a call-back rate of 5%. Thus, for this analysis, the sensitivity at the 95% specificity parameter was computed to estimate the approximate sensitivity for breast cancer screening using the PWMF observer.

The relationship between β and sensitivity at 95% specificity is shown in Figures 8 through 11 for simulated lesion diameters of 1 mm, 2 mm, 3 mm, and 5 mm, respectively. For these analyses, there were 130 breast data sets used for thin section images (shown in the (a) component of these figures) and there were 105 breast data sets used for thick projection

images. The lower number of data sets for the thick projection images were due to the elimination of some data sets (corresponding to small breasts) because a thick projection was not possible. Linear regression was performed and R^2 values are reported in Table II.

The R^2 values between β and sensitivity (at 95% specificity) reach a maximum for the 2–3 mm tumor diameters for the thin-section images. Since the simulation model used a pre-whitened matched filter with excellent detection performance (Packard et al., 2012), for larger tumors (as diameter $\rightarrow$ 5 mm) many of the AUC values reached 1.0 for the thin section (breast CT) data sets, and this horizontal line of accumulation at sensitivity = 1.0 can be seen for the 2, 3, and 5 mm lesion diameters in Figures 8a, 9a, and 10a, respectively. This asymptotic behavior in the individual sensitivity values resulted in a decrease in R^2 for the larger diameter lesions.

Using the same ROIs as for the computation of β, we also computed the fractal dimension, and this relationship is shown in Figure 12. The slope of the linear regression line was significantly different from zero ($p < 0.0001$), indicating a definite association between these two parameters. Increasing fractal dimension was associated with decreasing β. This is consistent with the work of Caldwell (Caldwell et al., 1990), Boone (Boone et al., 1998), and others, which showed that increasing fractal dimension is correlated with a reduction in breast density, implying an improvement in detection performance. Thus, the association of increasing fractal dimension with decreasing β gives additional evidence that lower values of β are associated with improved cancer detectability.

Discussion

Burgess (Burgess et al., 2001b) , Bochud (Bochud et al., 1997, Bochud et al., 1999), and others (Tischenko et al., 2005) have suggested that β, a parameter calculated from the anatomical noise power spectrum, is a metric which relates to the detectability of mass lesions in breast images. Specifically, it has been shown that lower values of β are associated with better detection performance. In this study, the goal was to establish a relationship between β and other known parameters which are associated with breast cancer detection performance. In short, the fundamental question addressed by this study is, "Does β matter?".

In Metheany *et al*, a relationship between thin slice breast images (breast CT) and thicker projection images (mammograms) was derived analytically, demonstrating that theoretically, the value of β for breast CT images is less than that of mammographic images by one: $\beta_{CT} = \beta_{mammo} - 1$ (Equation 3). This derivation, which exploited the dimensionality of the images, showed that thin slice images should have lower values of β than thicker projection images, but does not address the detection performance issue directly. The theoretical prediction was validated by experimental measurement (Chen et al, 2011).

In this current study, the value of β was associated with a number of parameters which are known to correlate with breast cancer detection performance. In Figure 2, the association between β and volume glandular fraction is illustrated, where lower values of β correspond to lower volume glandular fractions. Any clinical breast imager fully appreciates from their clinical experience the important role that breast density plays in the sensitivity of breast cancer detection, and this has been borne out in a number of publications as well (Fajardo et al., 1988, Pisano et al., 2005). While this relationship does not *prove* that lower values of β yield higher detection performance, it does demonstrate with high statistical significance that lower values of β are associated with lower glandular fractions, which in turn are known to be associated with better detection performance.

Figure 3a shows that as patients get older, the value of β decreases. This observation can be understood in the context of breast density, since breast density is known to decrease with increasing age. Similarly, Figure 3b illustrates that lower values of β are associated with larger breast diameters, and again, larger breast diameters are associated with over-weight and obese patients, with breast parenchymal patterns of lower density.

The detectability index (Figure 4–7) was shown to be highly associated with the value of β: that is, higher detectability index values correspond to lower values of β. This is illustrated in Figures 4 through 7 for simulated lesions of different diameters. These data also show the associations for both thin section and thick section breast images, and the trends in β and detection performance are consistent across thin and thick breast images. It is also observed that for similar values of β, thin section images have higher detectability indices than the thick section images, showing a potential different performance level between thin images (breast CT) and thicker projection (mammogram-like) images. All the associations between increased detectability index and decreased β were highly significant.

Figures 8 through 11 illustrate the relationship between sensitivity (at 95% specificity) and β. While the sensitivity metric tended to saturate at unity for the larger simulated breast lesion diameters, the trend demonstrating the decrease in sensitivity with an increase in the value of β was significant for both thin and thick section images, and for lesions ranging from 1 to 5 mm in diameter.

The relationship between β and fractal dimension (Figure 12) is not surprising, and decreasing values of β are associated with increased fractal dimension, which in turn is associated with lower breast density (Caldwell et al., 1990, Boone et al., 1998) and higher theoretical breast cancer detection levels.

In this work, the value of β has been demonstrated to be associated with numerous parameters which are well-known to be related to breast cancer detection performance. Most intuitive, breast density is highly associated with β, strongly suggesting by inference that lower values of beta correspond to increased detection performance in breast imaging. Breast density is one of the most highly discussed parameters which influence cancer detection performance in the literature, and it is also well appreciated by all radiologists who read breast images. The detectability index as well as diagnostic sensitivity determined from computer observer studies using a pre-whitened matched filter were also shown to correlate with statistical significance to lower values of β.

While an association between parameters is not proof of causality, the fact that β is associated with four semi-independent parameters (i.e., breast density, the detectability index, sensitivity, and the fractal dimension) which relate to breast cancer detectability is a more convincing demonstration of this hypothesis. In all cases, improved breast cancer detection performance is associated with a decrease in the value of β. The association between these parameters was demonstrated using linear regression techniques, however earlier theoretical analysis (Metheany *et al*.(Metheany et al., 2008)) also demonstrated from a first-principles argument that lower values of β correspond to increased breast cancer detection performance.

Conclusions

In this investigation, images of the breast generated using dedicated breast CT technology were used to evaluate mathematical descriptors which are thought to relate to breast cancer detectability. This study focused on mass lesions, and is not relevant to microcalcification-based lesions of the breast. The breast CT data sets were used intrinsically (thin section

images), and were also integrated to produce thick section images that are typical of mammography. While there are significant differences between integrated breast CT images and actual mammograms, previous studies have demonstrated that the value of β for mammograms and integrated (thick section) breast CT data are very similar (Chen et al., 2012). Using a number of computer-generated parameters including breast density, detectability index, sensitivity, and fractal dimension, the results of this investigation demonstrate conclusively that there is a strong association between lower values of β and parameters which are known to correlate with increased cancer detection performance. We summarize, based upon these statistically significant findings, that the value of β - a value derived from a power law fit to the anatomical noise power spectrum - can be considered as a surrogate measure of breast cancer detection performance. While causality has not and probably can never be demonstrated, the strong correlations and theoretical underpinnings of these relationships are unambiguous.

Acknowledgments

References

Barrett, HH.; Myers, K. Foundations of Image Science. Hoboken, New Jersey: John Wiley & Sons Inc.; 2004.

Bochud FO, Valley J-F, Verdun FR, Hessler C, Schnyder P. Estimation of the noisy component of anatomical backgrounds. Medical Physics. 1999; 26:1365–1370. [PubMed: 10435539]

Bochud, FO.; Verdun, FR.; Valley, J-F.; Hessler, C.; Moeckli, R. Importance of anatomical noise in mammography. In: Harold, LK., editor. SPIE 3036. 1997. p. 74-80.

Boone J, Lindfors K, Beatty C, Anthony seibert J. A breast density index for digital mammograms based on radiologists' randing. Journal of Digital Imaging. 1998; 11:101–115. [PubMed: 9718500]

Burgess, A.; Jacobson, F.; Judy, P. On the Difficulty of Detecting Tumors in Mammograms. In: Insana, M.; Leahy, R., editors. Information Processing in Medical Imaging. Berlin / Heidelberg: Springer; 2001a.

Burgess, AE. Mammographic structure: data preparation and spatial statistics analysis. In: Kenneth, MH., editor. SPIE 3661. 1999. p. 642-653.

Burgess AE, Jacobson FL, Judy PF. Human observer detection experiments with mammograms and power-law noise. Medical Physics. 2001b; 28:419–437. [PubMed: 11339738]

Burgess AE, Judy PF. Signal detection in power-law noise: effect of spectrum exponents. J. Opt. Soc. Am. A. 2007; 24:B52–B60.

Burton GJ, Moorhead IR. Color and spatial structure in natural scenes. Appl. Opt. 1987; 26:157–170. [PubMed: 20454092]

Caldwell CB, Stapleton SJ, Holdsworth DW, Jong RA, Weiser WJ, Cooke G, Yaffe MJ. Characterisation of mammographic parenchymal pattern by fractal dimension. Physics in Medicine and Biology. 1990; 35:235. [PubMed: 2315379]

Cargill EB, Donohoe KJ, Kolodny G, Parker AJ, Duane P. Estimation of fractal dimension of parenchymal organs based on power spectral analysis of nuclear medicine scans. Prog Clin Biol Res. 1991; 363:557–570. [PubMed: 1989001]

Chen L, Abbey CK, Nosrateih A, Lindfors KK, Boone JM. Anatomical complexity in breast parenchyma and its implications for optimal breast imaging strategies. Medical Physics. 2012; 39:1435–1441. [PubMed: 22380376]

Fajardo LL, Hillman BJ, Frey C. Correlation Between Breast Parenchymal Patterns and Mammographers' Certainty of Diagnosis. Investigative Radiology. 1988; 23:505–508. [PubMed: 3170137]

Feldkamp LA, Davis LC, Kress JW. Practical cone-beam algorithm. J. Opt. Soc. Am. A. 1984; 1:612–619.

Field DJ. Relations between the statistics of natural images and the response properties of cortical cells. J. Opt. Soc. Am. A. 1987; 4:2379–2394. [PubMed: 3430225]

Heine JJ, Deans SR, Velthuizen RP, Clarke LP. On the statistical nature of mammograms. Medical Physics. 1999; 26:2254–2265. [PubMed: 10587206]

Heine JJ, Velthuizen RP. Spectral analysis of full field digital mammography data. Medical Physics. 2002; 29:647–661. [PubMed: 12033559]

Huang S-Y, Boone JM, Yang K, Packard NJ, Mckenney SE, Prionas ND, Lindfors KK, Yaffe MJ. The characterization of breast anatomical metrics using dedicated breast CT. Medical Physics. 2011; 38:2180–2191. [PubMed: 21626952]

Kak, AC.; Slaney, M. Principles of Computerized Tomographic Imaging. New York: IEEE Press; 1988.

Lindfors KK, Boone JM, Nelson TR, Yang K, Kwan ALC, Miller DF. Dedicated Breast CT: Initial Clinical Experience. Radiology. 2008; 246:725–733. [PubMed: 18195383]

Metheany KG, Abbey CK, Packard N, Boone JM. Characterizing anatomical variability in breast CT images. Medical Physics. 2008; 35:4685–4694. [PubMed: 18975714]

Mettivier G, Russo P, Cesarelli M, Ospizio R, Passeggio G, Roscilli L, Pontoriere G, Rocco R. Dedicated scanner for laboratory investigations on cone-beam CT/SPECT imaging of the breast. Nuclear Instruments and Methods in Physics Research Section A: Accelerators, Spectrometers, Detectors and Associated Equipment. 2011; 629:350–356.

Mi ville FA, Bolard G, Bulling S, Gudinchet F, Bochud FO, Verdun FR. Effects of computing parameters and measurement locations on the estimation of 3D NPS in non-stationary MDCT images. Physica Medica.

Nelson TR, Cervino LI, Boone JM, Lindfors KK. Classification of breast computed tomography data. Medical Physics. 2008; 35:1078–1086. [PubMed: 18404942]

Packard, N.; Boone, JM. Glandular segmentation of cone beam breast CT volume images. In: Jiang, H.; Michael, JF., editors. SPIE 6510. 2007. p. 651038

Packard NJ, Abbey CK, Yang K, Boone JM. Effect of slice thickness on detectability in breast CT using a prewhitened matched filter and simulated mass lesions. Medical Physics. 2012; 39:1818–1830. [PubMed: 22482604]

Pisano ED, Gatsonis C, Hendrick E, Yaffe M, Baum JK, Acharyya S, Conant EF, Fajardo LL, Bassett L, D'orsi C, Jong R, Rebner M. Diagnostic Performance of Digital versus Film Mammography for Breast-Cancer Screening. New England Journal of Medicine. 2005; 353:1773–1783. [PubMed: 16169887]

Ruderman DL. The statistics of natural images. Network: Computation in Neural Systems. 1994; 5:517–548.

Tischenko O, Hoeschen C, Dance DR, Hunt RA, Maidment ADA, Bakic PR. Evaluation of a novel method of noise reduction using computer-simulated mammograms. Radiation Protection Dosimetry. 2005; 114:81–84. [PubMed: 15933085]

Tolhurst DJ, Tadmor Y, Chao T. Amplitude spectra of natural images. Ophthalmic Physiol Opt. 1992; 12:229–232. [PubMed: 1408179]

Van der schaaf A, Van hateren JH. Modelling the power spectra of natural images: Statistics and information. Vision Research. 1996; 36:2759–2770. [PubMed: 8917763]

Weigel M, Vollmar SV, Kalender WA. Spectral optimization for dedicated breast CT. Medical Physics. 2011; 38:114–124. [PubMed: 21361181]

Yaffe MJ, Boone JM, Packard N, Alonzo-proulx O, Huang S-Y, Peressotti CL, Al-mayah A, Brock K. The myth of the 50–50 breast. Medical Physics. 2009; 36:5437–5443. [PubMed: 20095256]

Yang K, Kwan AL, Huang SY, Packard NJ, Boone JM. Noise power properties of a cone-beam CT system for breast cancer detection. Med Phys. 2008; 35:5317–5327. [PubMed: 19175091]
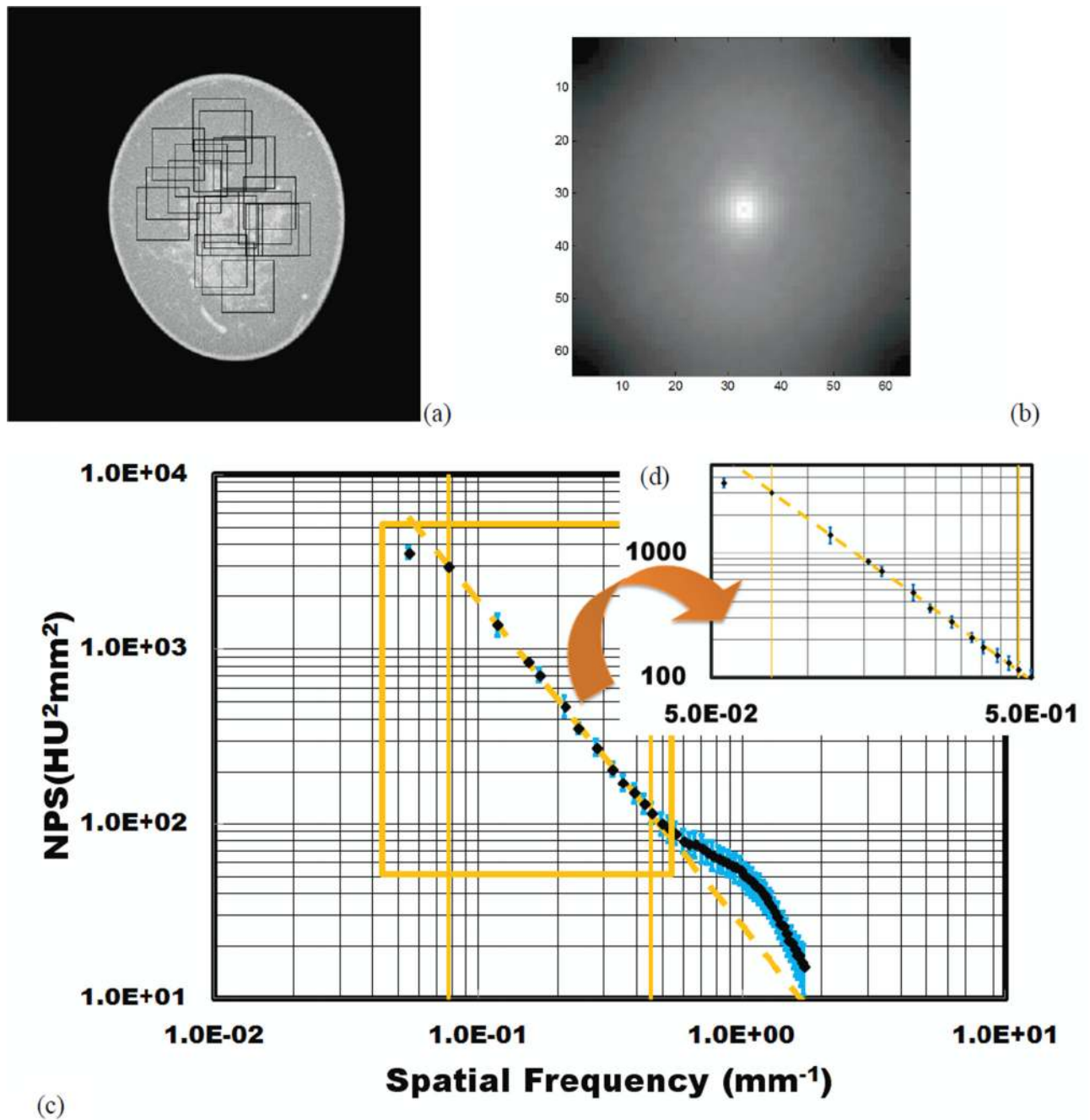
Figure 1.
The experimental method for computing the noise power spectrum is illustrated graphically.
(a) One thousand regions of interest are placed on each breast volume data set, and two-dimensional ROI's are extracted.
(b) After detrending and Hanning filter application, the two-dimensional Fourier transform is computed resulting in the 2-D noise power spectrum.
(c) The NPS is radially integrated, producing a one-dimensional plot of the NPS as a function of spatial frequency. A subsection of this data is used for the computation of β.

(d) As described in the text, upper and lower frequency windows were used to identify the most linear portion of the anatomical NPS, based upon R^2. The values of α and β were computed in this region for each breast data set.
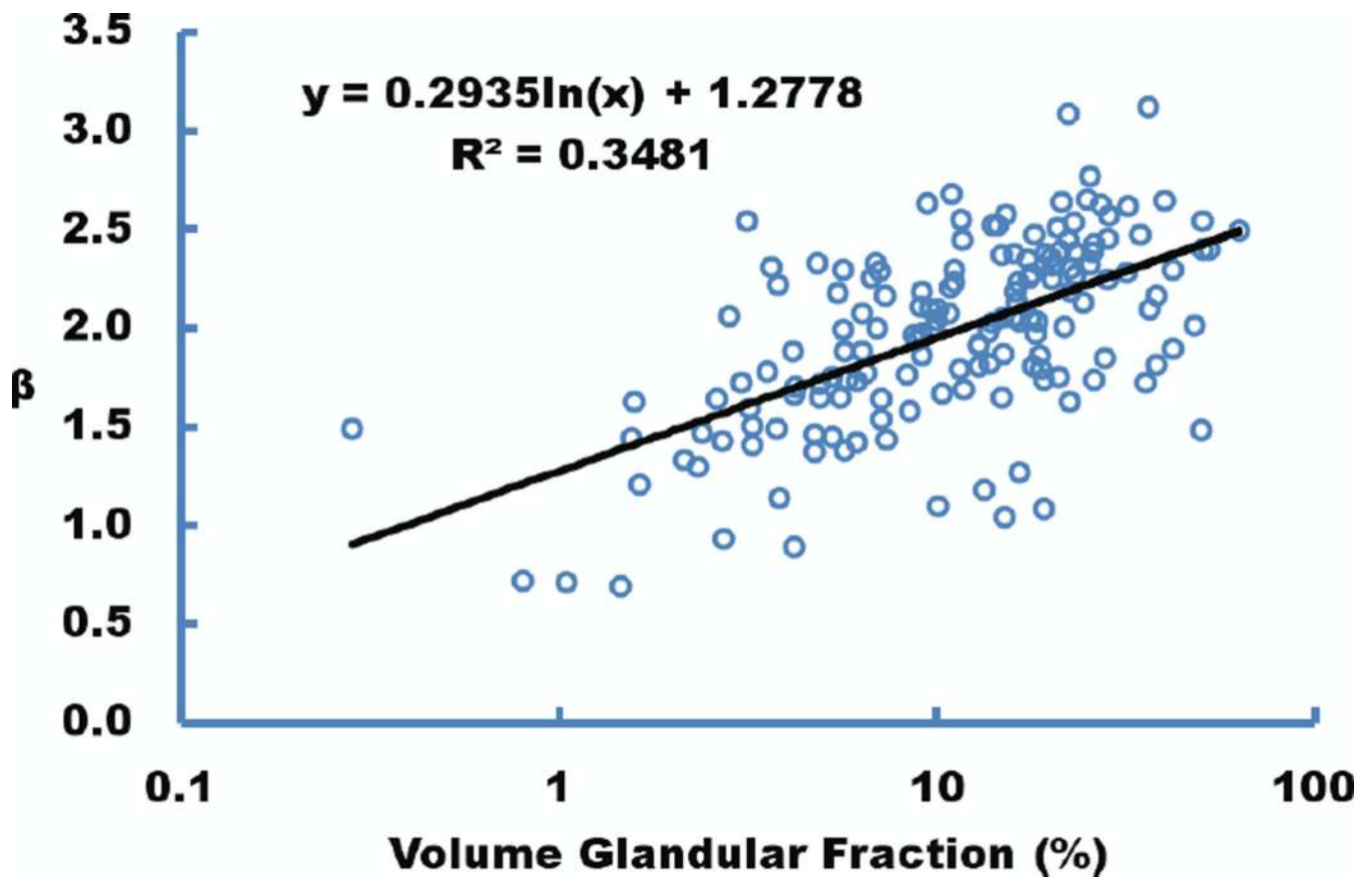
Figure 2.
The value of β is plotted as a function of volume glandular fraction (VGF), showing a trend of increasing beta with increasing VGF. It is well recognized that increasing breast density (VGF) corresponds to a reduction in sensitivity for breast cancer identification, and this plot suggests that increasing values of β are also associated with less efficient breast cancer identification.
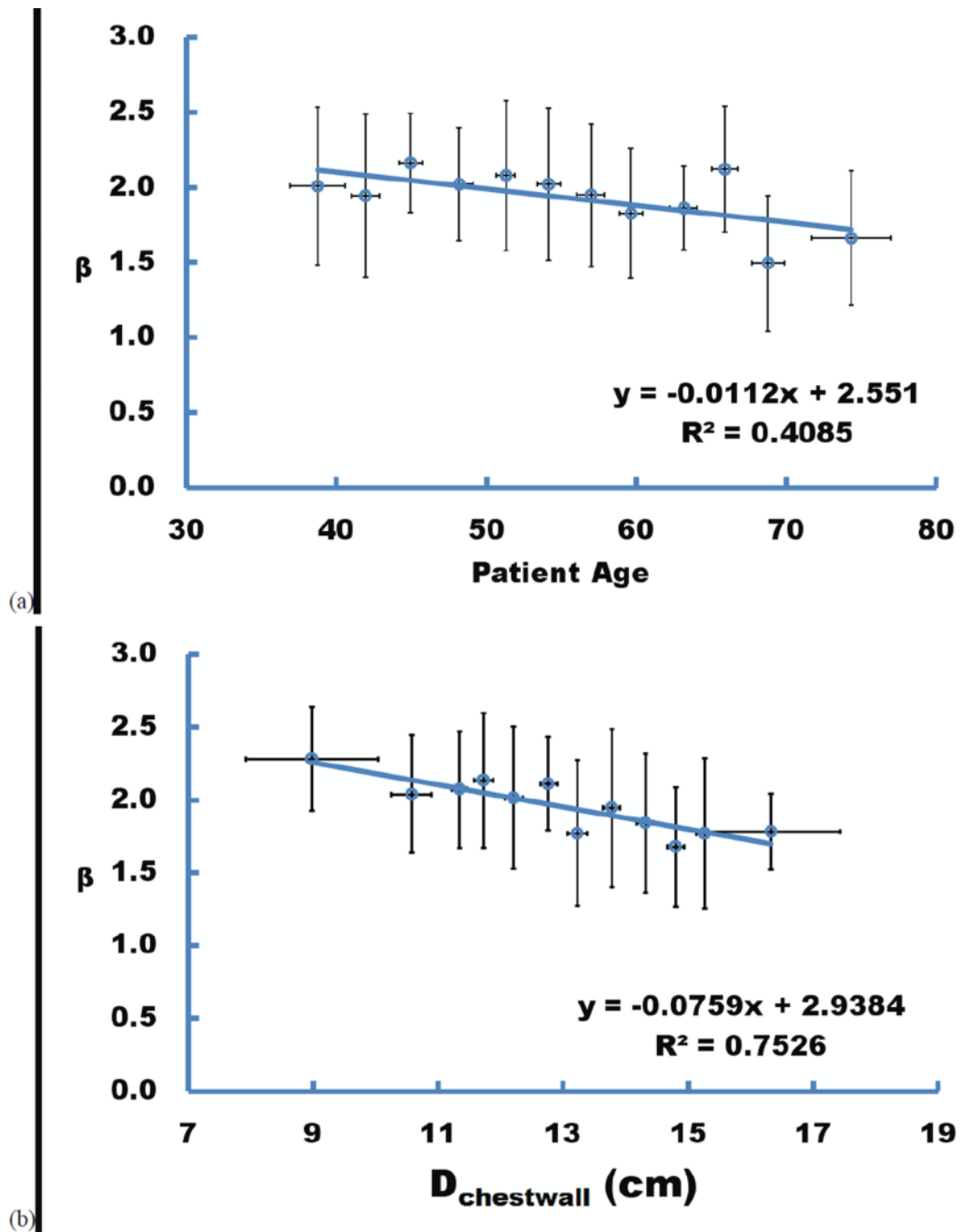
Figure 3.
(a) The value of β is plotted as a function of patient page, where 12 different categories were used to smooth the data. Increasing age corresponds to a reduction in breast density, which corresponds to an increase in sensitivity and a decrease in the measured value of β.
(b) The value of β is plotted as a function of breast diameter at the chest wall, $D_{chestwall}$. Increasing breast diameter is generally associated with increasing patient obesity, lower breast density, and again a reduction in β is seen.

(a)
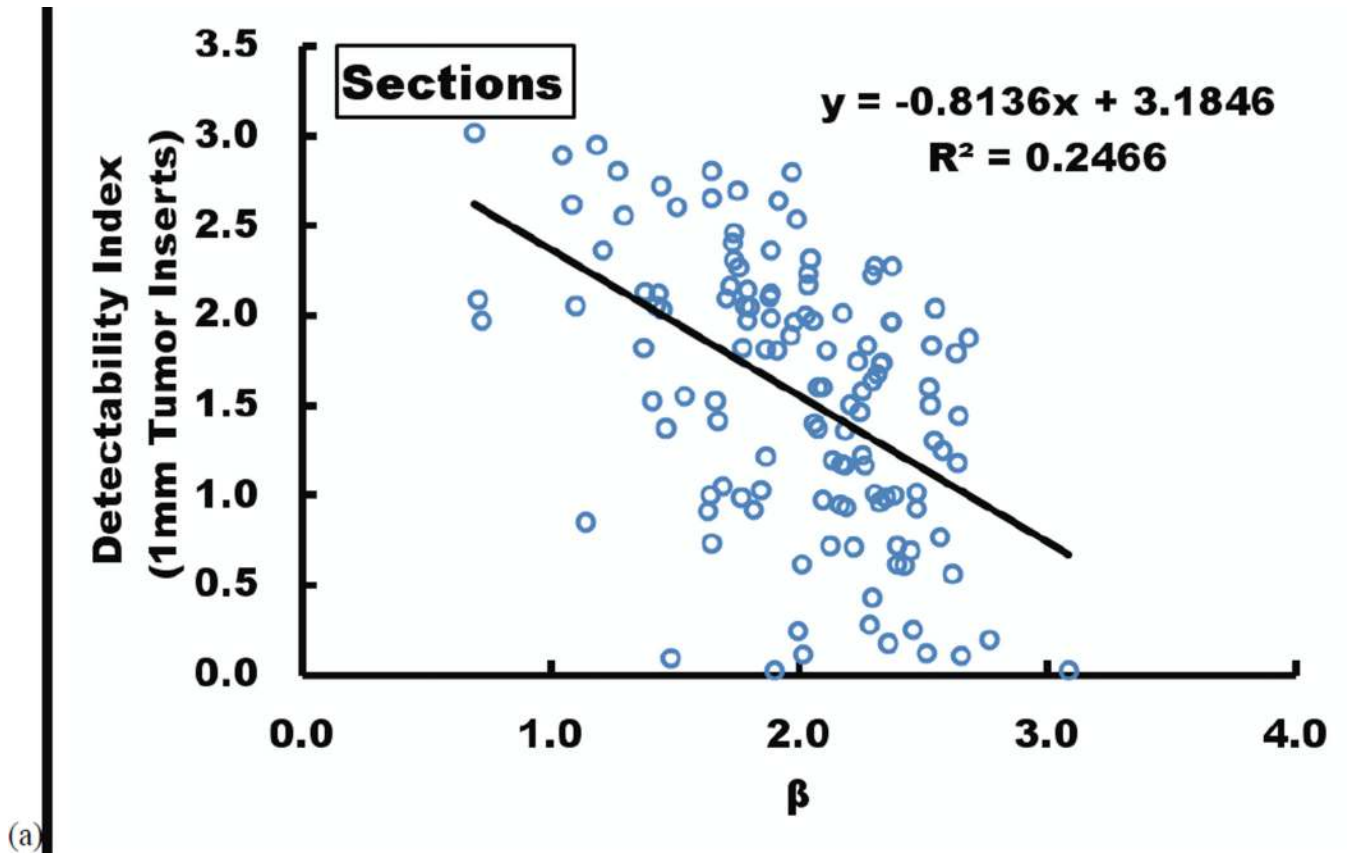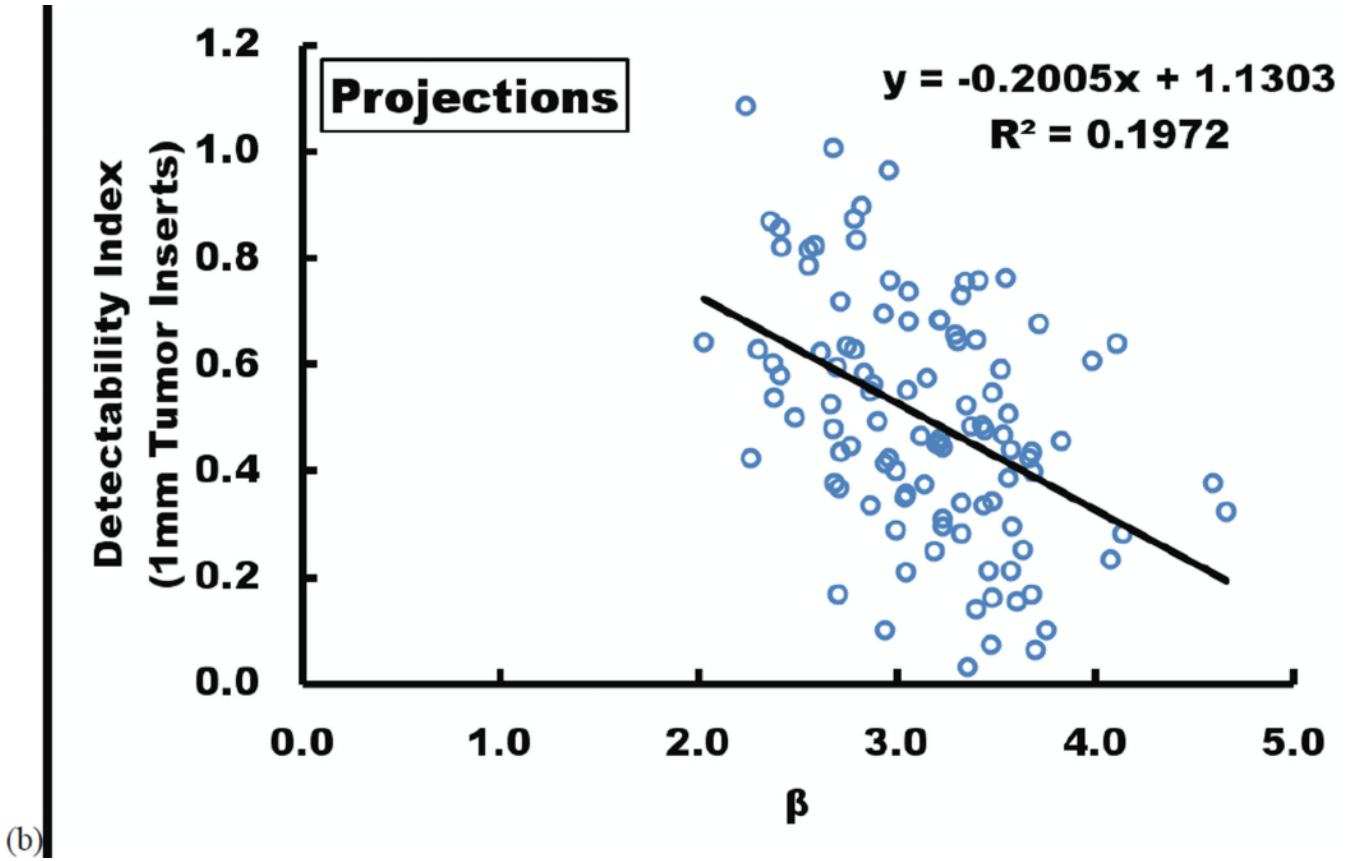
Figure 4.
(a) The detectability index for 1 mm diameter computer-simulated tumors is shown as a function of β. Increased detectability is associated with lower values of β based upon these data. These data represent the breast CT thin section data.
(b) Again, the detectability index is illustrated as a function of β, with higher detectability being associated with lower values of β. These data are for the (thick) projection images, which are computed by averaging breast CT slices together. These trends illustrate that lower values of β correspond to increase detection performance for mammogram-like images.
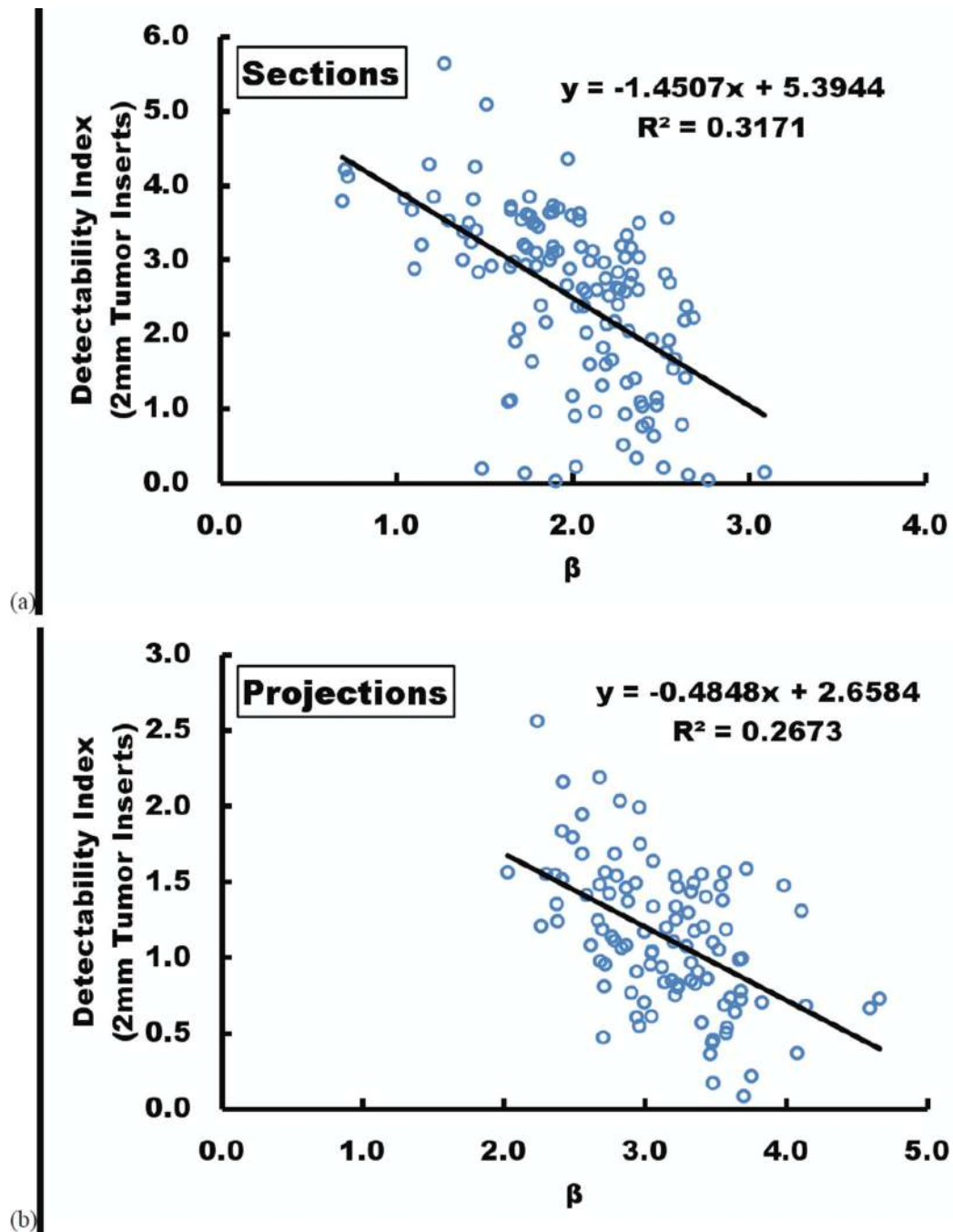
Figure 5.
(a) The detectability index for 2 mm simulated lesions is illustrated as a function of β, again illustrating a negative slope which indicates that lower values of β correspond to higher detectability levels. These data are for thin section breast CT images.
(b) These data are for thick section projection images, and also show that lower values of β correspond to improved detection performance.
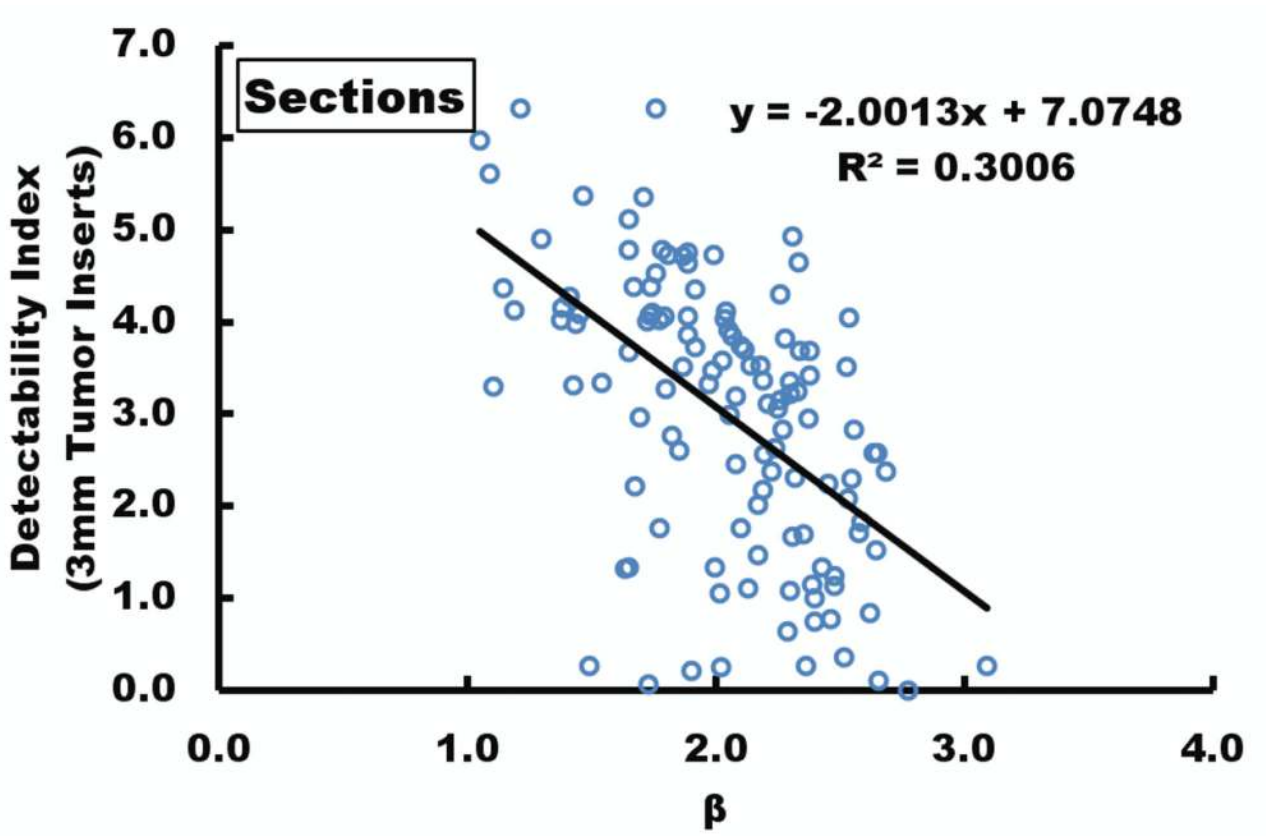
(a)
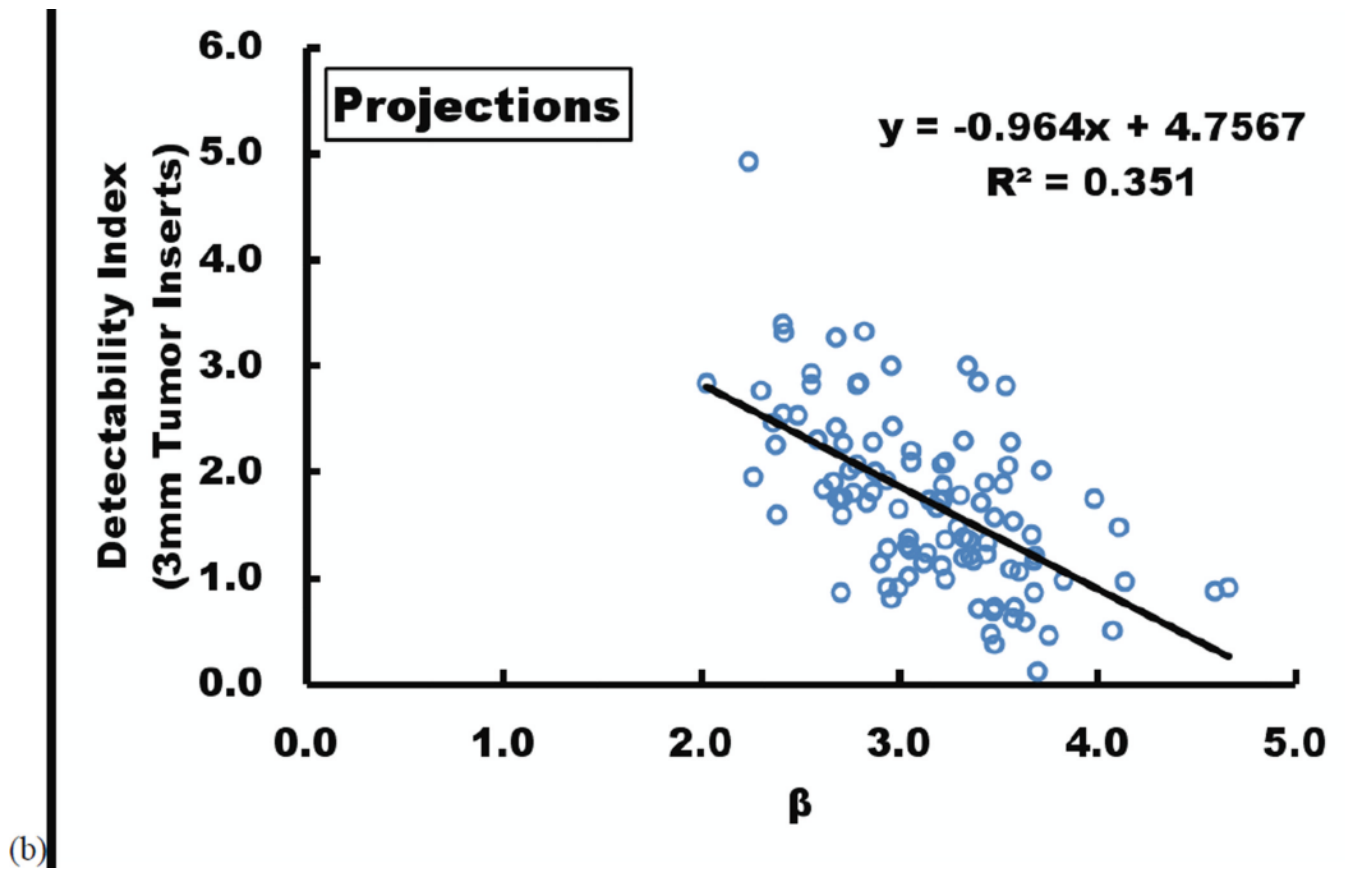
Figure 6.
(a) This figure, shown for thin section CT images with 3 mm simulated lesions, demonstrate the trends illustrated in the prior two figures.
(b) This figure corresponds to projection images with 3 mm simulated lesions, and also illustrates the reduction in detectability index as β increases.
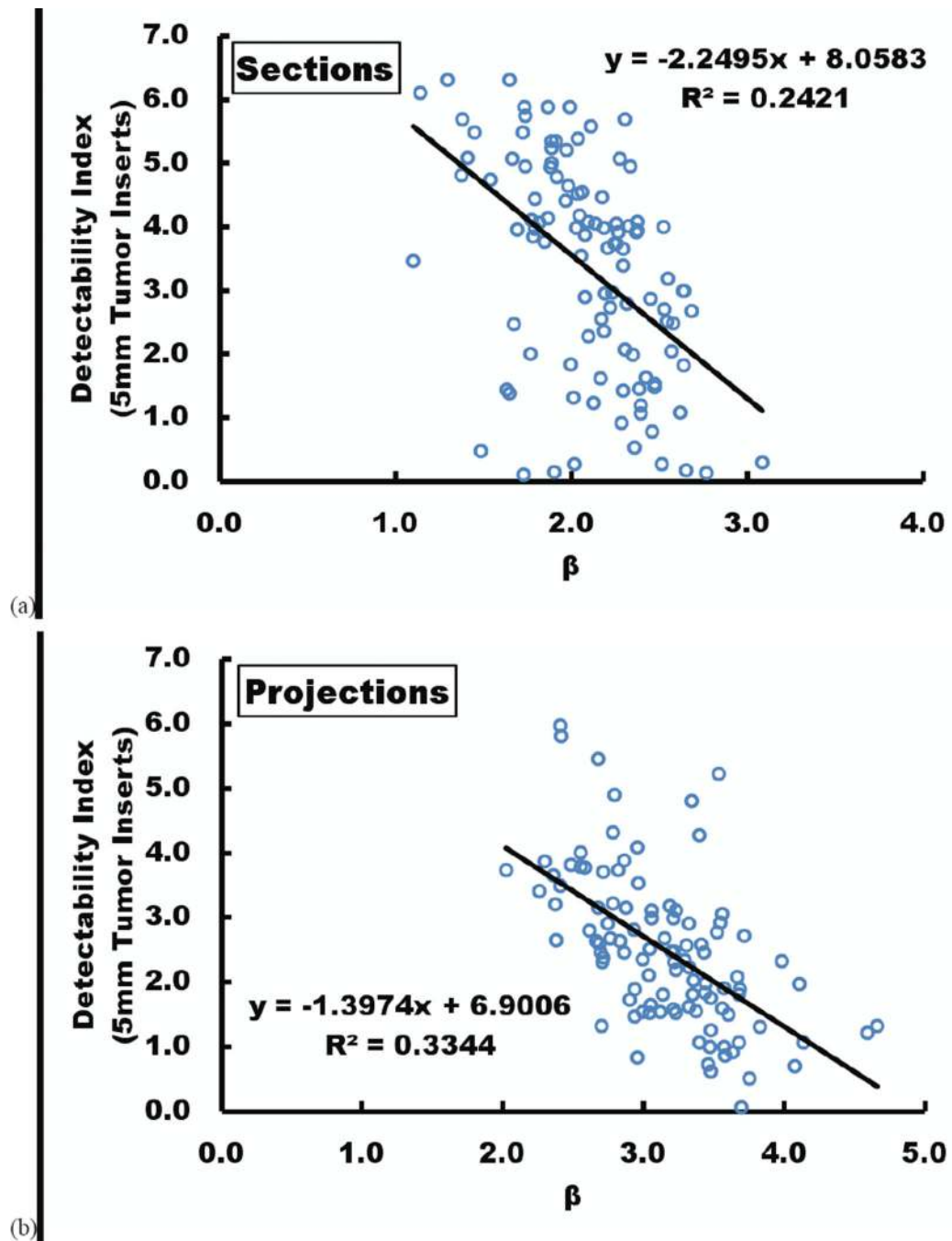
Figure 7.
(a) The detectability index for 5 mm simulated spherical lesions is illustrated as a function of data for thin section breast CT images. This figure echoes Figures 2 through 6, and illustrate the correlation between increased detectability index with lower values of β.
(b) This figure shows the same trends as in Figure 7a, except for thick section projection images.
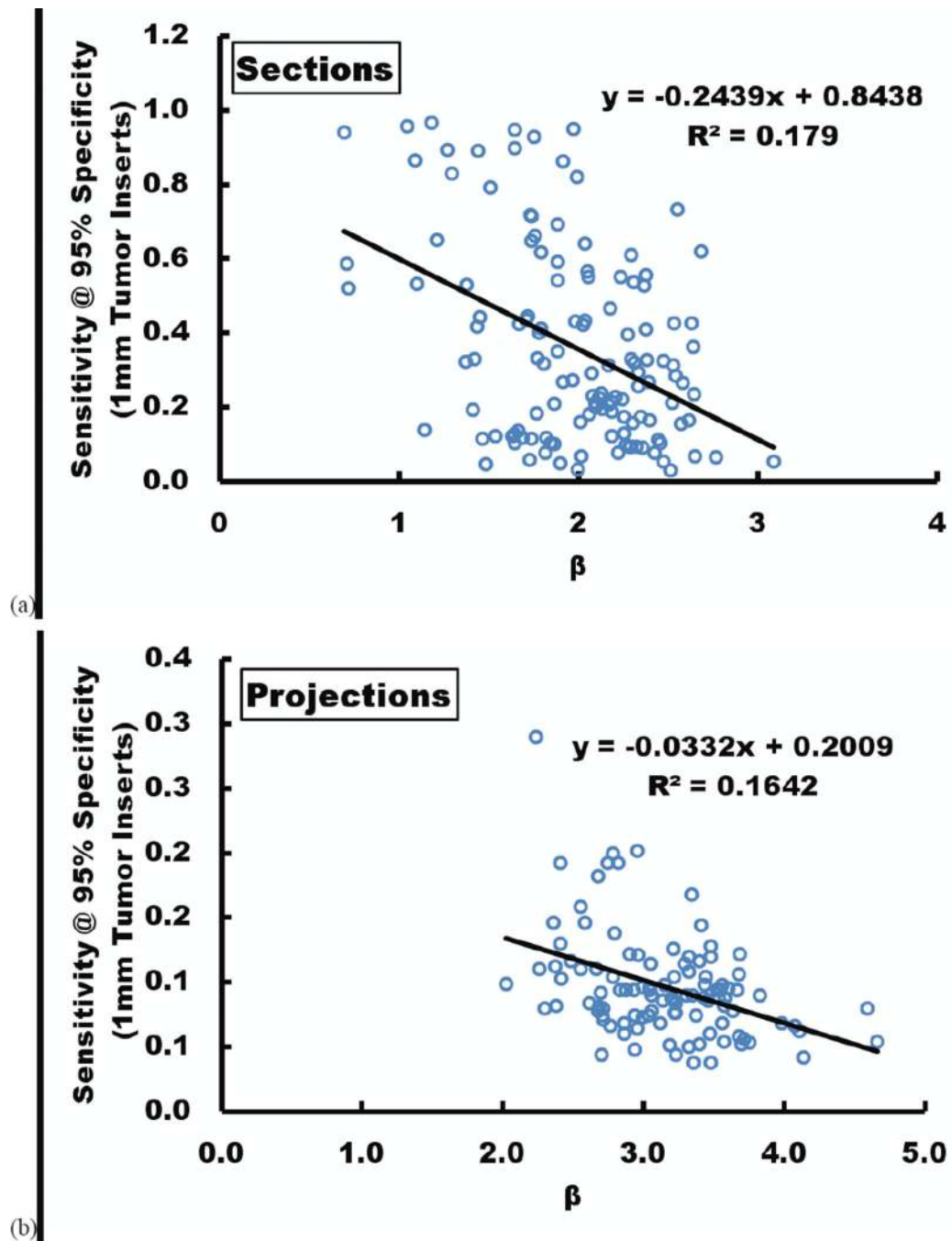
Figure 8.
(a) The sensitivity at 95% specificity is illustrated using simulated tumors, as a function of β. Demonstrating a similar trend to the detectability index, lower values of β are correlated with higher measures of sensitivity based upon computer simulated lesions. These data are for thin section CT images.
(b) The same trend as in Figure 8A is seen here, for projection (mammogram-like) images.
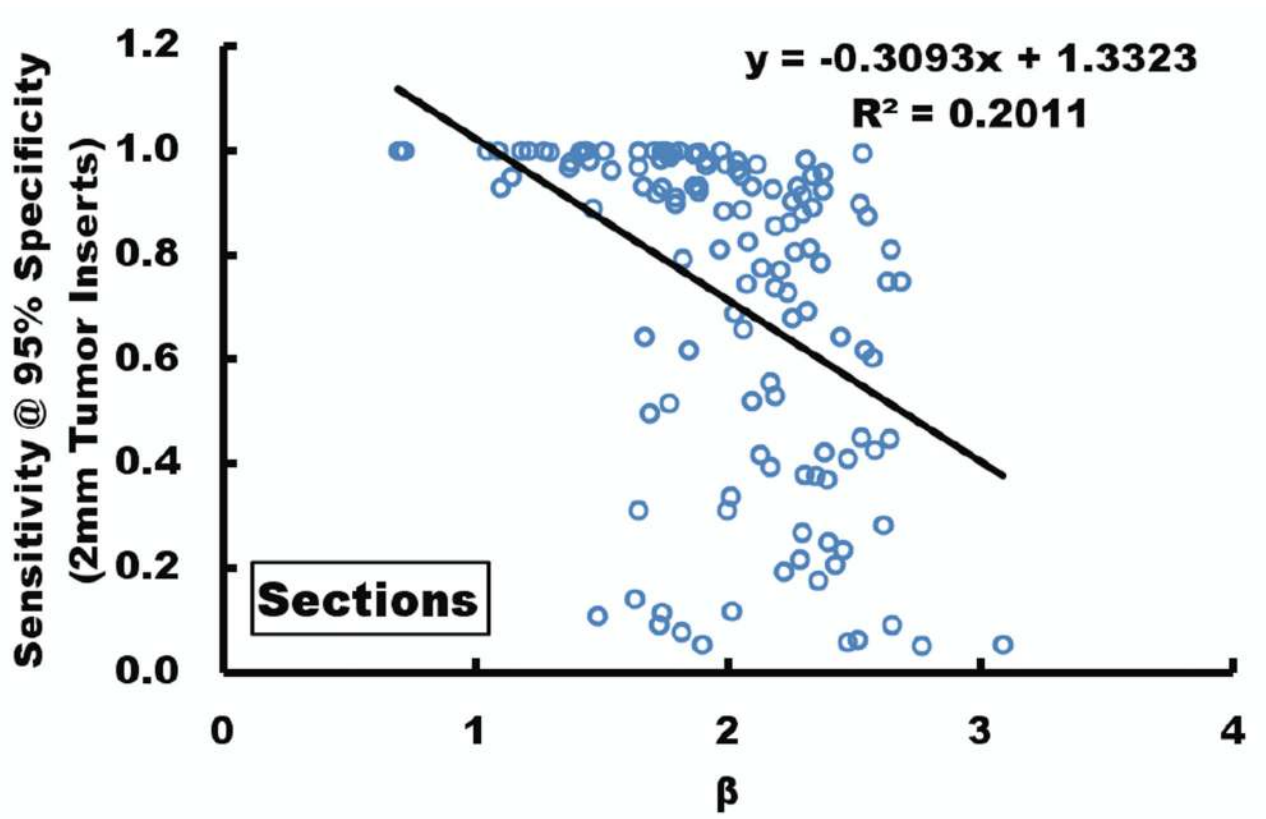
(a)
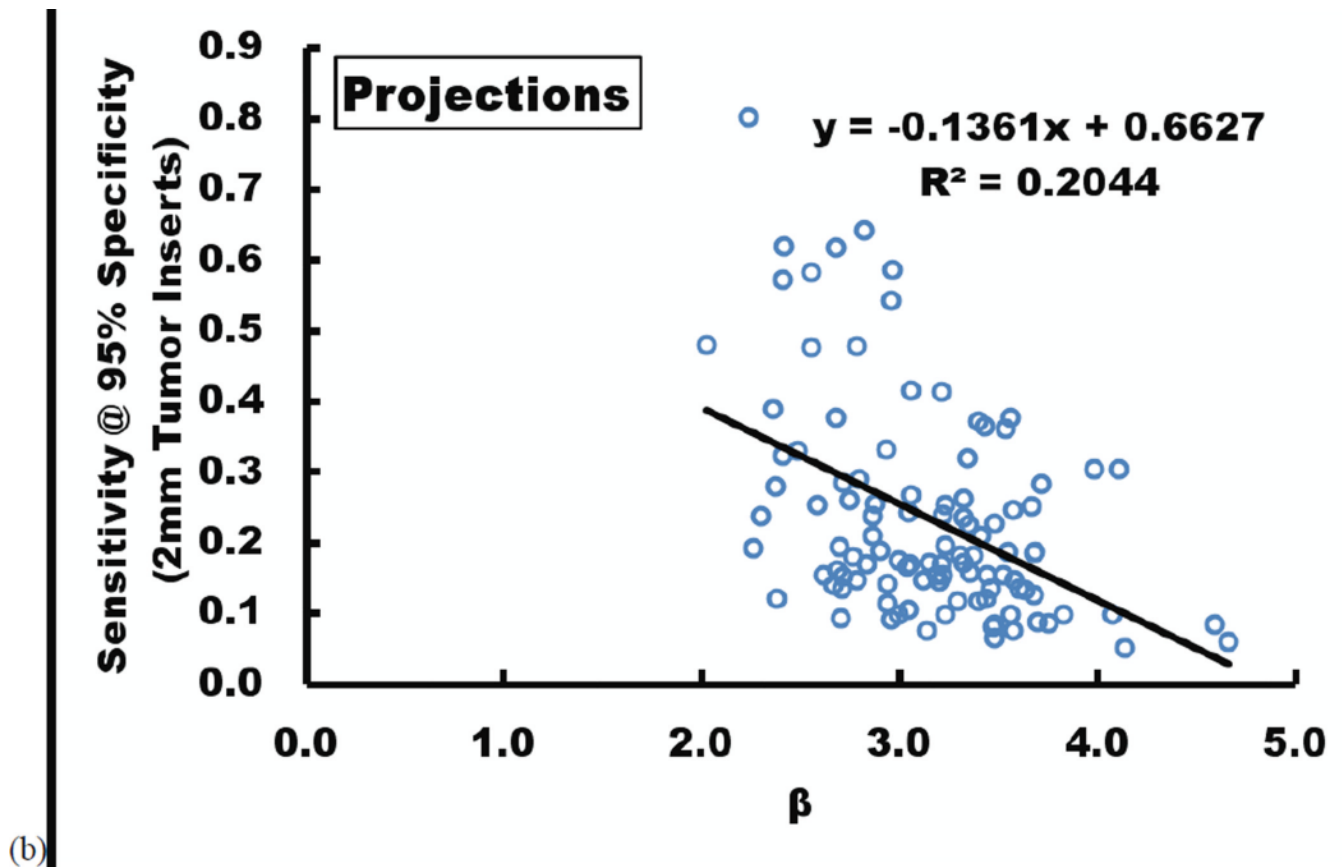
Figure 9.
(a) The sensitivity at 95% specificity is illustrated for 2 mm simulated lesions as a function of β. Here, the sensitivity in many of the data sets approach to 100%, as indicated by the grouping of data points horizontally at sensitivity = 1.0. Lower values of β are associated with improvements in sensitivity for these thin section breast CT images.
(b) For thick section images, similar trends are seen as in the case for the thin section breast CT images.
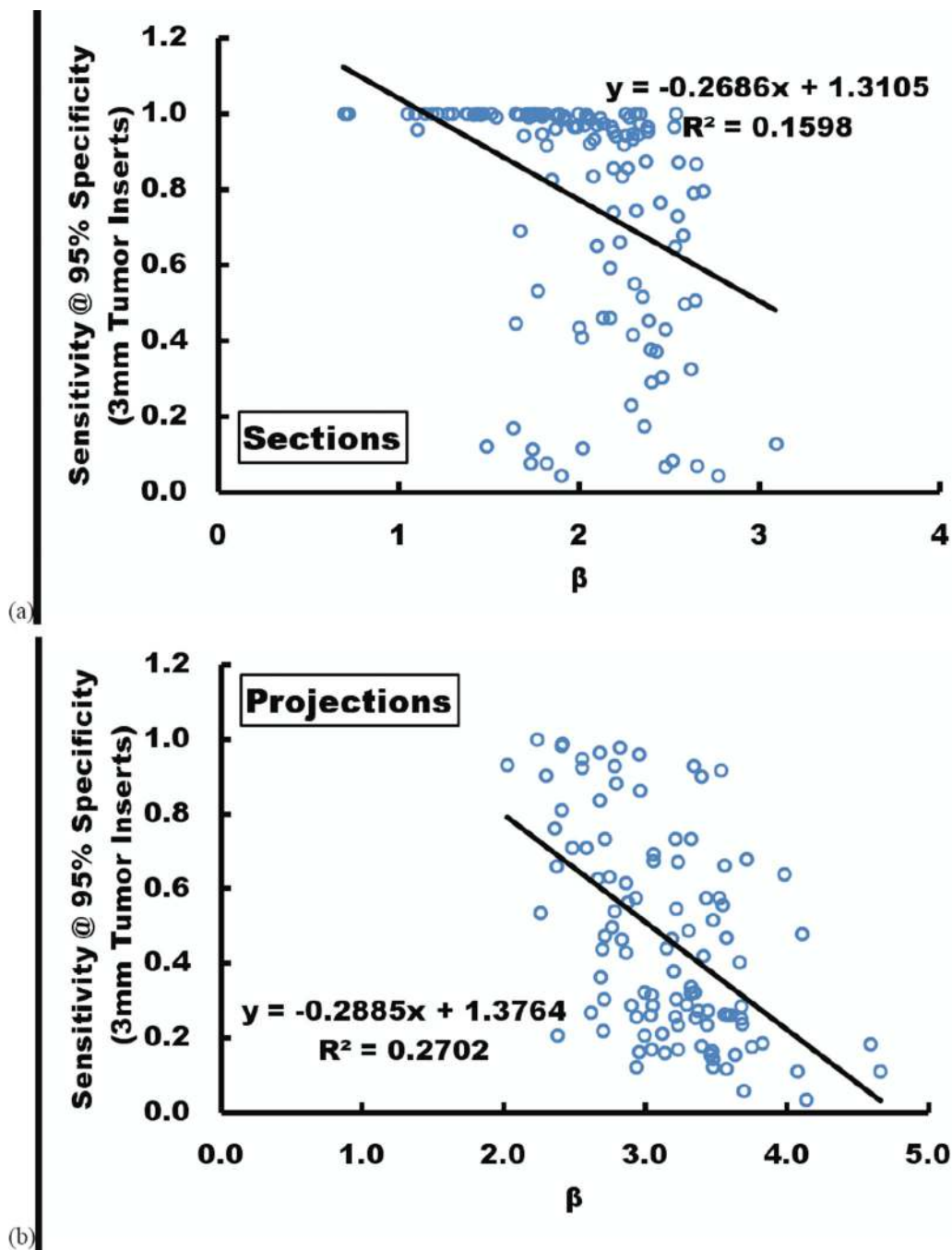
Figure 10.
(a) This figure illustrates the reduction in sensitivity as a function of increasing β, for simulated mass lesions of 3 mm in diameter for thin section breast CT images.
(b) This figure illustrates, for thicker projection images, that decreasing sensitivity occurs at higher values of β

(a)

(b)
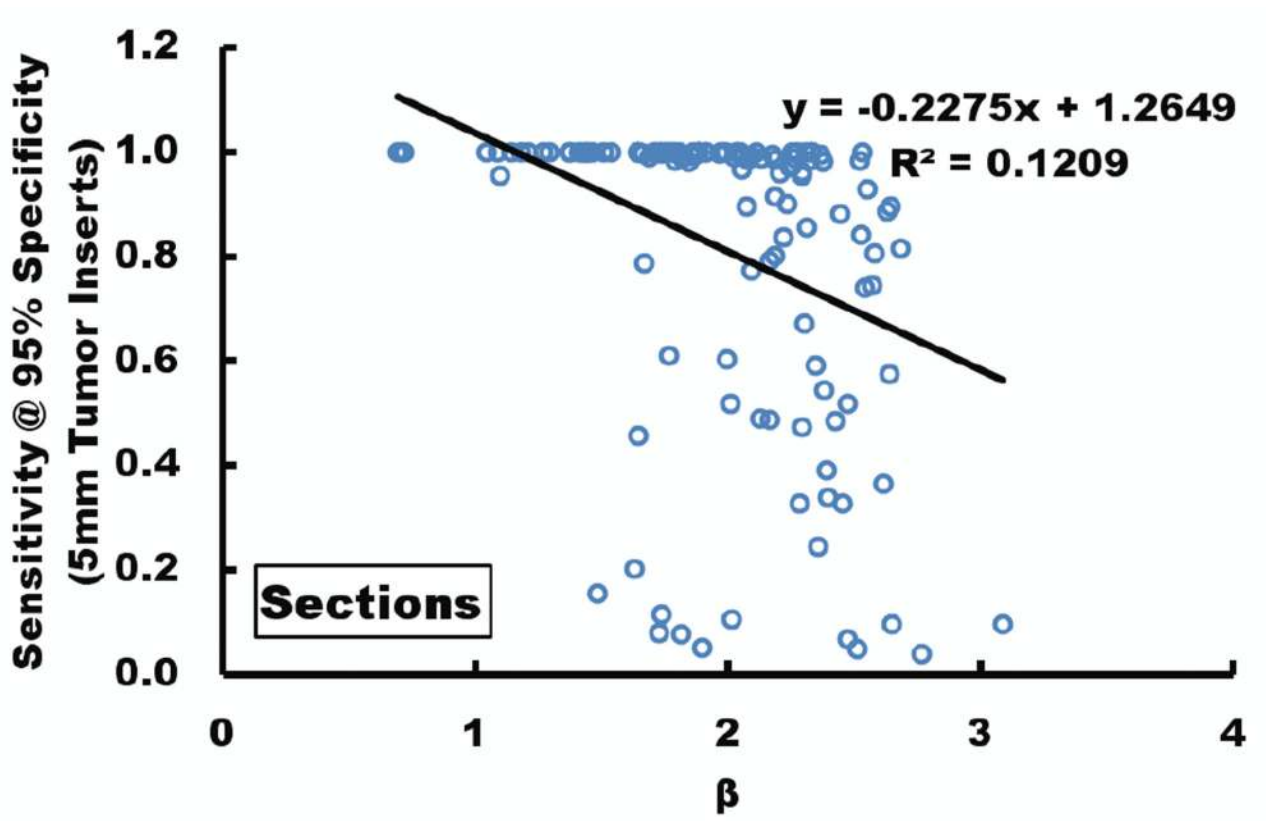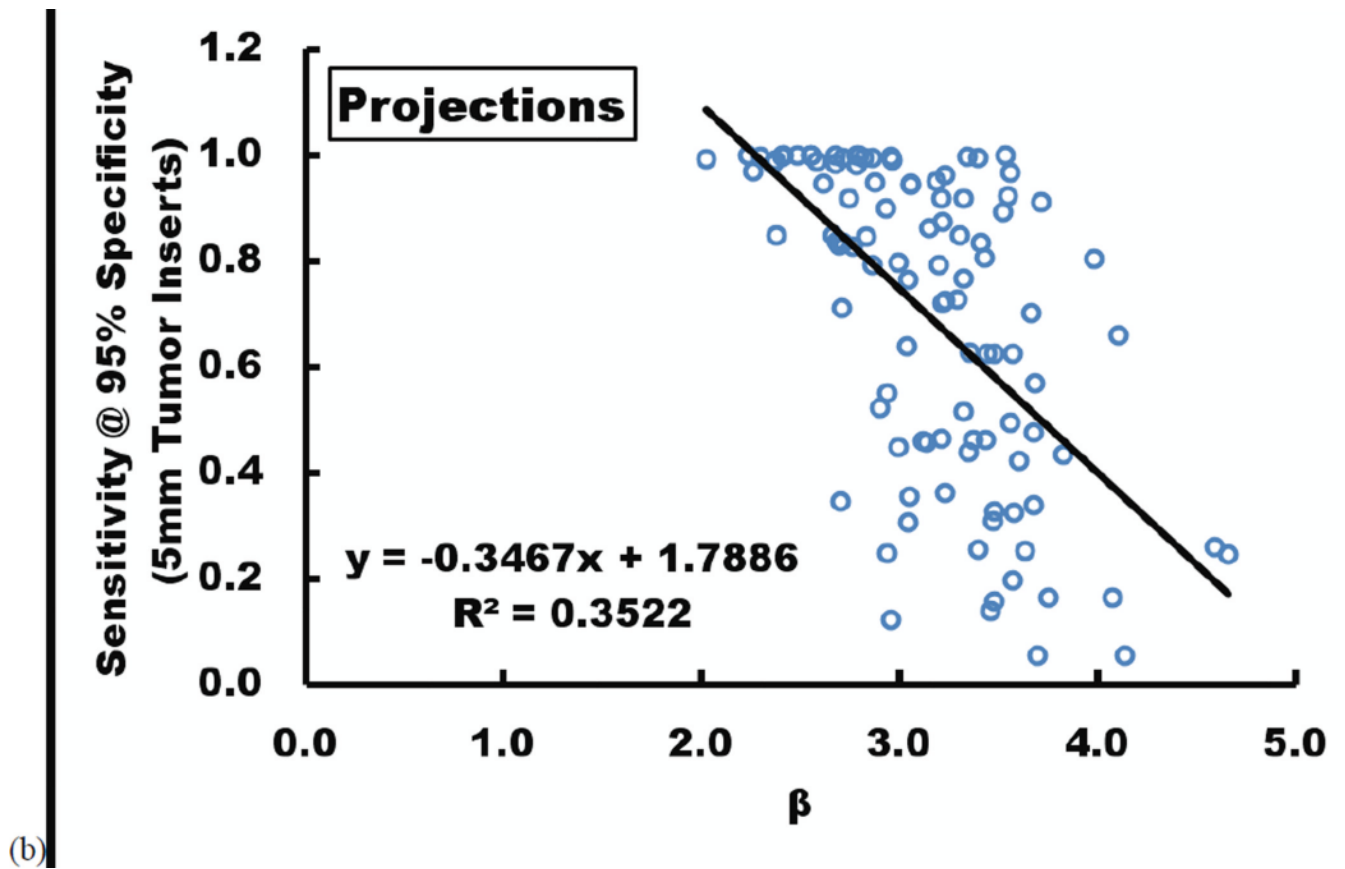
Figure 11.
(a) This figure illustrates that sensitivity decreases as a function of increasing β, for simulated mass lesions of 5 mm in diameter for thin section breast CT images.
(b) This figure illustrates, for thicker projection images, that decreasing sensitivity occurs at higher values of β.
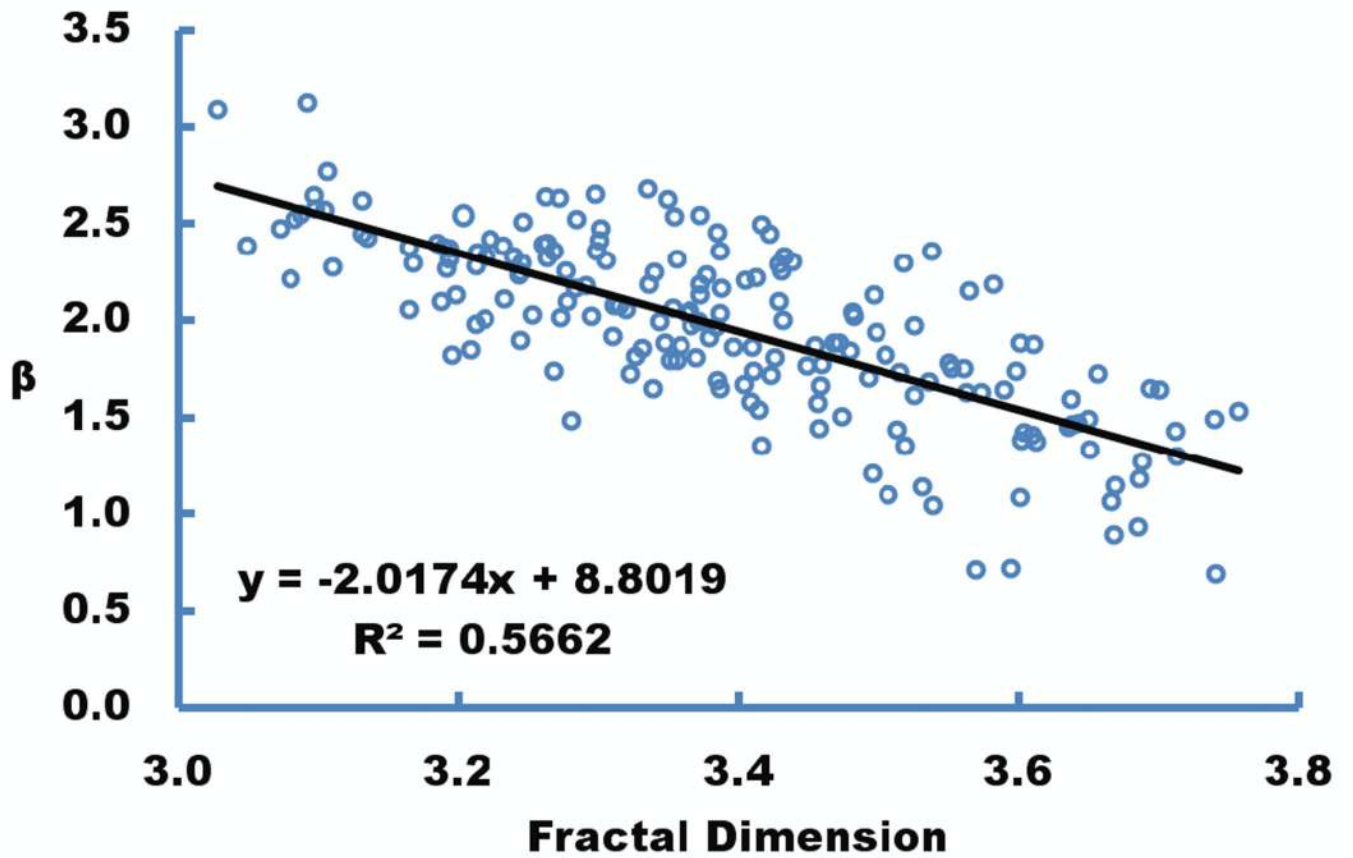
Figure 12.
As recognized by a number of authors, the value of β is related mathematically to the fractal dimension. This figure shows that lower fractal dimension is associated with higher values of β.

Table 1

This table shows the number of data sets (and), the correlation coefficient, and the associated P value for both thin sections (corresponding to breast CT images) and thick sections (corresponding to mammogram like images), as a function of computer simulated lesion diameter. In all cases, the slope of each figure is significantly different from zero, indicating that the trend between increasing detectability and decreasing beta is significant.

Lesion Diameter (mm)	Thin Sections (t ~ 0.23 mm)			Thick Projections (t ~ 44.8 mm)		
	N	R²	P-value	N	R²	P-value
1	127	0.2466	<0.0001	105	0.1972	<0.0001
2	128	0.3171	<0.0001	105	0.2673	<0.0001
3	121	0.3006	<0.0001	105	0.3510	<0.0001
5	107	0.2421	<0.0001	104	0.3344	<0.0001

Table.2

This table illustrates the parameters associated with the fit between sensitivity at 95% specificity and β. Across four computer-simulated lesion diameters, for both thin sections and thick sections, there was a significant difference between the slope of the relationship and zero.

Lesion Diameter (mm)	Thin Sections (t ~ 0.23 mm) 130 breasts		Thick Projections (t ~ 44.8 mm) 105 breasts	
	R^2	P-value	R^2	P-value
1	0.1790	<0.0001	0.1642	<0.0001
2	0.2011	<0.0001	0.2044	<0.0001
3	0.1598	<0.0001	0.2702	<0.0001
5	0.1209	<0.0001	0.3522	<0.0001